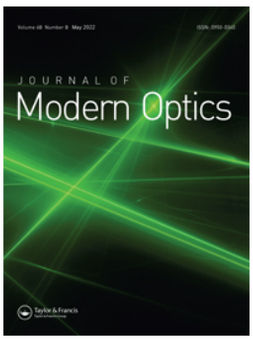

Journal of Modern Optics

ISSN: (Print) (Online) Journal homepage: https://www.tandfonline.com/loi/tmop20

Performance comparison of commonly used photoacoustic tomography reconstruction algorithms under various blurring conditions

Pankaj Warbal & Ratan K. Saha

To cite this article: Pankaj Warbal & Ratan K. Saha (2022) Performance comparison of commonly used photoacoustic tomography reconstruction algorithms under various blurring conditions, Journal of Modern Optics, 69:9, 487-501, DOI: 10.1080/09500340.2022.2053598

To link to this article: https://doi.org/10.1080/09500340.2022.2053598

Published online: 31 Mar 2022.

JOURNAL OF MODERN OPTICS
2022, VOL. 69, NO. 9, 487–501
https://doi.org/10.1080/09500340.2022.2053598

Taylor & Francis
Taylor & Francis Group

Performance comparison of commonly used photoacoustic tomography reconstruction algorithms under various blurring conditions

Pankaj Warbal and Ratan K. Saha

Department of Applied Sciences, Indian Institute of Information Technology Allahabad, Prayagraj, India

ABSTRACT

A reconstructed image in photoacoustic tomography (PAT) imaging modality can be blurred because of some system-dependent effects – broad laser pulse, the limited bandwidth of the sensors, acoustically attenuating medium and transducers with finite-size apertures having Gaussian sensitivity profile. A robust deblurring method involving a system matrix is presented in this work. Image reconstruction was accomplished by using the backprojection (BP), interpolated time reversal (ITR), Tikhonov regularization (TH) and total variation minimization (TV) schemes. A modified version of the BP algorithm was also explored for image reconstruction for finite transducers. Each factor of blurring was considered at a time. For the model-based methods, the system matrix was constructed in presence of such a factor. Subsequently, the model matrix inversion method was deployed for image formation. Quantitative values of some standard metrics were computed to assess the performance of the reconstruction protocols. The visual inspection of the reconstructed images as well as numerical values of the figures of merit revealed that the BP and ITR techniques generally fail to remove blurring; however, the model-based methods can provide distortion-free images under various conditions. For example, the numerical values of the Pearson correlation coefficient (PCC) for all the cases showed a strong correlation between the nominal and reconstructed images for the TH and TV techniques compared to the BP and ITR methods. The TV method can be utilized in practice to facilitate the PAT image reconstruction free from system-dependent blurring.

ARTICLE HISTORY
Received 18 May 2021
Accepted 9 March 2022

KEYWORDS
Photoacoustic tomography; deblurring; system matrix; reconstruction

1. Introduction

Photoacoustic imaging (PAI) is a hybrid imaging modality that combines the advantages of optical and ultrasound imaging techniques in a single modality. The PA tomography (PAT) imaging modality has diverse areas of applications such as sentinel lymph node imaging, blood vasculature and molecular imaging, tumour angiogenesis, breast imaging and brain imaging in small animals and so on [1–5]. PAT image reconstruction can be performed using analytical approaches referred to as the backprojection and time reversal algorithms [6–8]. These methods require a full view data set for faithful imaging of the ground truth. They are fast and simple in general but quantitatively less accurate. For the limited view data set, it is worthy to apply the model-based techniques for reconstruction [4,9–12]. These methods are computationally expensive but give fairly accurate results. The Tikhonov regularization is one such approach that has been extensively used for PAT reconstruction.

There are four common sources of blurring in PAT imaging. These are (i) finite temporal width of the incident laser pulse, (ii) finite bandwidth of the detectors, (iii) acoustically absorbing and dispersive coupling medium and (iv) transducers with finite-size apertures. In case of finite pulse width, the condition of stress confinement is not obeyed. The source and the surrounding extracellular matrix both contribute to the generation of the pressure signals. As a result of that, a thin source behaves like an extended object giving rise to blurring in the reconstructed image. In the second case, narrow bandwidth detectors only receive low-frequency signals. Therefore, sharpness of the edges of the object is lost causing image blurring. Similarly, in the third case, high-frequency waves are absorbed within the ambient medium during propagation from the source to the detectors. Loss of high-frequency signals is responsible for image blurring. In the fourth case, a transducer with finite aperture transforms an input delta pressure pulse into a broad pulse. Consequently, the reconstructed image becomes blurry and also tangential resolution degrades radially (with respect to the imaging centre).

CONTACT Ratan K. Saha ratank.saha@iiita.ac.in Department of Applied Sciences, Indian Institute of Information Technology Allahabad, Prayagraj 211 015, India

Many studies have been conducted to remove or reduce the amount of blurring from PAT images. For example, Wang et al., deconvolved one-dimensional PA signals with that of a point source and then a modified filtered backprojection algorithm was used for image reconstruction [13]. The deconvolution procedure removed the effect of the impulse response of the acoustic transducer and consequently, reconstructed images exhibited good agreement with the original phantoms. The Wiener filtering of the measured one-dimensional PA signals before image reconstruction was also found to improve the quality of the PAT images [14]. Rejesh et al. utilized a deconvolution method for reducing blurring, produced by finite width of the input laser pulse and finite bandwidth of the detectors, from PAT images [15]. The effect of absorbing medium on the PAT image reconstruction has been widely studied by many groups [16–18]. These studies suggest that image reconstruction should be performed after compensation of frequency-dependent acoustic attenuation loss to minimize image distortion.

Li et al. and Roitner et al. designed special deconvolution filters for deblurring (blurring occurs due to finite size of the apertures of the detectors) [19,20]. Van et al. compared the performance of various deconvolution filters in PAT imaging [21]. Recently, a modified delay and sum algorithm has been developed to address the same issue [22]. In this approach, the PA signal captured by a finite transducer was distributed on several points lying on the recording surface. This step was repeated for all transducers and then the delay and sum algorithm was implemented. The validity of the algorithm was tested under different apodization conditions of the sensor as well [23]. The properties of ultrasonic transducers can be loaded into the system matrix and after that image formation can be performed [24,25]. Chowdhury et al. considered the role of the coupling medium (between the curved-array elements and the tissue medium) in PAT imaging [26].

The construction and inversion of the system/model matrix are computationally intensive tasks. However, it is a single-step and universal process for correcting the image distortions originating from different system-dependent factors. The deconvolution-based methods [13–15,19,20] practically do not pose any computational burden but involve two steps – a deconvolution operation is performed first on one-dimensional signals and then image reconstruction is carried out. Moreover, this approach needs different deconvolution filters to mitigate different system-dependent factors. Therefore, the system/model matrix approach seems to be universally appealing.

The objectives of this work are to (a) explicitly and systematically consider the blurring conditions (for the light source, detectors and the medium) while generating the PA signals (forward data), (b) build a system matrix by incorporating each blurring condition at a time for image reconstruction using the l_2 and l_1 norm-based regularization methods and (c) compare the performance of these regularization algorithms with the analytical techniques. Therefore, the major significance of this work is to build a system matrix for each blurring factor. In particular, to the best of our knowledge, constructions of system matrix for a lossy and dispersive medium as well as for apodized transducers have not been performed so far. These have leaded to improved PAT imaging.

The image reconstruction for model-based protocols is carried out by employing the matrix inversion approach [27–29]. During this procedure, the system-dependent parameters inducing blurring are expected to be cancelled out and thus system-independent imaging may be possible. To test this hypothesis, numerical experiments for PAT imaging have been performed in the presence of four blurring factors (one at a time). The backprojection (BP), interpolated time reversal (ITR), Tikhonov (TH) regularization and total variation minimization (TV) algorithms have been implemented for image reconstruction when the PA signals have been detected by the point sensors. However, BP, modified BP (abbreviated as MBP and is a variant of the BP algorithm), TH and TV methods have been deployed for image formation when the PA signals have been captured by transducers with finite apertures. Numerical values of some standard metrics have been computed to quantitatively assess the performance of these algorithms. Our numerical results demonstrate that the TH and TV methods can be implemented in practice to form PAT images devoid of system-dependent blurring.

2. Theoretical models

2.1. Modelling of the PA wave propagation

2.1.1. Wave propagation in a lossless medium

Consider that a biological tissue containing chromophores is excited with a delta function, $\delta(t)$, laser pulse. The equation representing the acoustic wave generation and propagation through an acoustically lossless and nondispersive medium is given by [6],

$$\nabla^2 p(\mathbf{r},t) - \frac{1}{v^2}\frac{\partial^2 p(\mathbf{r},t)}{\partial t^2} = -\frac{p_0(\mathbf{r})}{v^2}\frac{\mathrm{d}\delta(t)}{\mathrm{d}t}, \qquad (1)$$

where v is the speed of sound of the medium and $p_0(\mathbf{r})$ is the initial pressure build up within the imaging region.

Various methods are available to solve Equation (1), namely, pseudo-spectral method [7], finite element method [30], Green's function approach [31], etc. In PAT, we map the initial pressure rise, i.e. $p(\mathbf{r}, t)$ at $t = 0$ or $p_0(\mathbf{r})$ within the imaging region from measured boundary data set.

2.1.2. Wave propagation in a lossy and dispersive medium

The PA waves undergo attenuation when it travels through biological tissue. The acoustic attenuation is, in general, frequency dependent, and the attenuation coefficient (α) can be modelled as [18]

$$\alpha = \alpha_0 \omega^{\gamma}, \tag{2}$$

where ω is the angular frequency; α_0 and γ are the prefactor and exponent for the power law, respectively. The unit of α_0 is Np $(\text{rad/s})^{-\gamma}\,\text{m}^{-1}$; numerical value of γ typically lies between 1 and 2 for biological tissue.

As the phase velocity of acoustic waves varies with frequency, the acoustic attenuation is often followed by the dispersion of those waves. As a result of that, the shape of a propagating pulse changes [18]. The Kramers–Kronig relations connect the frequency-dependent attenuation and the dispersion [32]. A general dispersion relation satisfying Equation (2) can be written as [33]

$$k(\omega) = \frac{\omega}{v} + i\alpha_0 |\omega|^{\gamma} + \alpha_0 \tan(\pi\gamma/2)\, \omega |\omega|^{\gamma-1}, \tag{3}$$

where $k(\omega)$ is the frequency-dependent wave number. The corresponding time-independent wave equation becomes

$$[\nabla^2 + k^2(\omega)] p(\mathbf{r}) = 0. \tag{4}$$

The solution to Equation (4) can be obtained using the Green's function approach. The appropriate Green's function in 3D becomes [7]

$$\begin{aligned} G(\mathbf{r}, \mathbf{r}_0) &= \frac{e^{ik(\omega)|\mathbf{r}-\mathbf{r}_0|}}{4\pi|\mathbf{r}-\mathbf{r}_0|}, \\ &= \frac{e^{i\omega|\mathbf{r}-\mathbf{r}_0|/v}}{4\pi|\mathbf{r}-\mathbf{r}_0|} e^{-\alpha_0|\mathbf{r}-\mathbf{r}_0|(|\omega|^{\gamma} - i\tan(\pi\gamma/2)\,\omega|\omega|^{\gamma-1})}, \end{aligned} \tag{5}$$

where $\mathbf{r}$ and $\mathbf{r}_0$ are the source and field points, respectively. The second exponential term in Equation (5) is responsible for attenuation and dispersion of the acoustic wave while propagating through the medium.

2.2. Image reconstruction algorithms

2.2.1. Analytical approaches

Let us consider $p(\mathbf{r}_0, t)$ is the pressure measured at $\mathbf{r}_0$ at time t. The universal BP formula for image reconstruction in terms of $p(\mathbf{r}_0, t)$ written as [6]

$$p_0^b(\mathbf{r}) = \int_{\Omega_0} b\left(\mathbf{r}_0, t = \frac{|\mathbf{r}-\mathbf{r}_0|}{v}\right) \mathrm{d}\Omega_0 / \Omega_0, \tag{6}$$

where $b(\mathbf{r}_0, t)$ is the BP term and is given by

$$b(\mathbf{r}_0, t) = 2p(\mathbf{r}_0, t) - 2t\frac{\partial}{\partial t} p(\mathbf{r}_0, t), \tag{7}$$

and the detection element dS_0 subtends a solid angle of $\mathrm{d}\Omega_0$ at $\mathbf{r}$. The total solid angle subtended by the whole detection surface at point $\mathbf{r}$ is denoted by Ω_0. Only the first term of Equation (7) has been considered (for simplicity) herein during the implementation of Equation (6) for image reconstruction.

Note that $p(\mathbf{r}_0, t)$ is the pressure measured by a point detector positioned at $\mathbf{r}_0$ at time t. However, a realistic detector has a finite size. The impinging pressure waves become spatially averaged due to the finite aperture effect and hence, the collective signal (over the surface area S) can be expressed as [23]

$$p'(\mathbf{r}_0, t) = \int_S p(\mathbf{r}_0', t)\, W(\mathbf{r}_0') d^2\mathbf{r}_0', \tag{8}$$

where $W(\mathbf{r}_0')$ is the sensitivity profile of the detector. It can be taken as [23]

$$W(\mathbf{r}_0') = \begin{cases} 1, & \text{when the profile is uniform} \\ e^{-\dfrac{|\mathbf{r}_0' - \mathbf{r}_0|^2}{2\sigma^2}}, & \text{when the profile is Gaussian} \end{cases} \tag{9}$$

where σ is the standard deviation for the Gaussian apodization function and $\mathbf{r}_0$ denotes the centre of the detector. One can use the resultant signals [i.e. Equation (8)] detected by the sensors with finite apertures for image reconstruction via the BP algorithm. The spatial averaging of the PA signals for finite detectors introduces blurring in the reconstructed images. The amount of blurring can be reduced by decreasing σ of the Gaussian apodization function [23]. In this work, a finite detector (a line element in two dimensions) has been broken into many points and the resultant signal (recorded by that detector) has been distributed in the same Gaussian manner over those points [34]. After that, the conventional BP algorithm has been applied for image reconstruction. This is termed as the MBP algorithm, which has been found to remove blurring effectively.

The TR algorithm can be used to determine $p_0(\mathbf{r})$ inside the imaging region [7]. It assumes that the medium is acoustically homogeneous. It first performs the forward simulation up to time $t = T$ and records PA pressure at the detector locations. After that, it numerically solves the time-dependent wave equation in the backward time direction considering measured data as the boundary constrain. The spatial map of pressure at $t = 0$ can be treated as the reconstructed image. The number of detectors can be increased using an interpolation scheme before performing the inverse simulation to improve image reconstruction.

2.2.2. System matrix approaches

The forward model for the PAT imaging can be cast in terms of a system of linear equations as [35]

$$\mathrm{A}z = b, \tag{10}$$

with $A \in \mathbb{R}^{m\times n}$, $b \in \mathbb{R}^m$ and $z \in \mathbb{R}^n$. Here, A is the system/model matrix [11]. It contains responses of all the pixels present inside the imaging region at the detector locations. The vector b is the pressure data measured at the boundary and z is the map of initial pressure rise. A unique solution for Equation (10) exists when $m = n$ and it can be obtained easily. Unique solution does not exist if $m \neq n$.

Equation (10) can be solved utilizing the TH method. In this case, the following cost function is minimized [11,36]:

$$\Sigma = ||\mathrm{A}z - b||_2^2 + \lambda^2||Lz||_2^2, \tag{11}$$

where λ is the regularization parameter and L is the regularization matrix (they control the smoothness of the solution); $||.||_2$ is the l_2 norm. The identity matrix (I) is the standard choice for L. The solution to Equation (11) for $L = I$ becomes

$$z_{TH} = (\mathrm{A}^T\mathrm{A} + \lambda\mathrm{I})^{-1}\mathrm{A}^T b, \tag{12}$$

where T is the transpose operation for a matrix. The choice of the appropriate regularization parameter is an important factor of the TH scheme. The reconstruction result depends on this parameter, which is known to filter out some of the natural features present in the actual image.

The total variation minimization method can also be employed to solve Equation (10). Here, the cost function looks like [37]

$$\Sigma = \frac{\eta}{2}||\mathrm{A}z - b||_2^2 + \sum_i ||D_i z||_1, \tag{13}$$

where D_i is the discrete gradient operator on z at the ith position. Note that η is the primary penalty term (a positive quantity). In this work, image reconstruction has been performed exploring the TH and TV protocols.

2.3. Quantitative assessment of the reconstruction schemes

Some image quality parameters have been computed to assess the performance of the reconstruction schemes. They are briefly described here.

Error norm (ERN): The ERN can be estimated by computing the following formula [25]:

$$\mathrm{ERN} = ||z - z_r||_2, \tag{14}$$

where z and z_r are the nominal and estimated values, respectively. ERN becomes zero when z and z_r are identical.

Pearson correlation coefficient (PCC): The PCC can be defined as [25]

$$\mathrm{PCC} = \frac{\mathrm{COV}(z, z_r)}{\xi_z \xi_{z_r}}, \tag{15}$$

where COV, ξ_z and ξ_{z_r} are the covariance between two image matrices, standard deviation of z and standard deviation of z_r, respectively. It quantifies the similarity between the actual and the reconstructed images. The PCC value varies from –1 to 1. Better reconstructions have higher PCC values.

Contrast to noise ratio (CNR): The formula for calculating the CNR is [38]

$$\mathrm{CNR} = \frac{\mu_{roi} - \mu_{back}}{(\xi_{roi}^2 n_{roi} + \xi_{back}^2 n_{back})^{\frac{1}{2}}}, \tag{16}$$

where, 'roi' and 'back' are the source and background regions of the reconstructed image as shown in Figure 1(b). Here, μ and ξ represent the mean and standard deviation, respectively; $n_{roi} = A_{roi}/A_{total}$ and $n_{back} = A_{back}/A_{total}$ where A_{roi} and A_{back} are the total number of pixels in the actual image with $p_0 \neq 0$ and $p_0 = 0$, respectively; A_{total} is the total number of pixels in the original/reconstructed image.

Signal to noise ratio (SNR): The SNR can be computed from [11]

$$\mathrm{SNR} = 20\log_{10}\left(\frac{M}{\xi_{back}}\right), \tag{17}$$

where M is the peak value of pressure in the 'roi'.

Structure similarity index (SSIM): The SSIM is used to measure the similarity of the reconstructed image with

respect to the source. The SSIM can be computed using the following equation as [39]

$$\mathrm{SSIM} = \frac{(2\mu_z\mu_{z_r} + c_1)(2\,\mathrm{COV}(z, z_r) + c_2)}{(\mu_z^2 + \mu_{z_r}^2 + c_1)(\xi_z^2 + \xi_{z_r}^2 + c_2)}, \qquad (18)$$

where c_1 and c_2 are the variables to stabilize the above equation in case of weak denominator.

3. Simulation methodology

3.1. Forward simulation

The k-Wave toolbox was utilized to compute the PA signals [7]. Figure 1(a) shows the schematic of the simulation setup in 2D. A vasculature phantom as shown in Figure 1(b) was considered in this study. The size of the computational domain was 1101 × 1101 grid points. The length of each pixel was 0.1 mm. An absorbing layer of width 2 mm was placed to wrap the computational domain. A total of 80 detectors (denoted by red solid circles in Figure 1a) were circularly placed over an angle 2π at a distance of 50 mm from the centre of the simulation domain. The size of the imaging region was 20×20 mm^2 (consisting of 201×201 grid points). The density and the speed of sound of the medium were taken as 1000 kg/m^3 and 1500 m/s, respectively. The numerical phantom was loaded occupying the imaging region and then the forward simulation was performed. The PA signals were acquired by the detectors. For each PA signal, pressure data for 2500 time points with an interval of 20 ns were recorded. A 40-dB noise was added to such a signal (using AddNoise function of the k-Wave toolbox). The forward simulation code was executed in a virtual machine (RAM: 256 GB, cores: 80, clock speed: 2.19 GHz, processor: Intel Core (Skylake, IBRS), OS: CentOS). The execution time was about 17 minutes.

Four different types of simulations were conducted in this study. At first, the width of the input Gaussian light pulse was sequentially increased (300, 600 and 900 ns) and accordingly, the PA signals were generated. Generally, PAT imaging is done using 10 ns laser pulses from Nd:YAG lasers. For pulsed laser diodes, the pulse width is of the order of 400 ns [15]. The detectors were considered point detectors with centre frequency 2.25 MHz and 70% bandwidth. The medium was treated as acoustically lossless and nondispersive. In the second case, we took a delta function light pulse and point detectors with 2.25 MHz as the centre frequency. However, the bandwidth was gradually elevated (30%, 50% and 90%). The standard choice for PAT imaging is 70% bandwidth. In the third case, medium properties were varied as $\alpha_0 = 0.75$ dB MHz$^{-\gamma}$cm^{-1} and $\gamma = 1.5$, $\alpha_0 = 5.75$ dB MHz$^{-\gamma}$cm^{-1} and $\gamma = 1.5$ and $\alpha_0 = 3.75$ dB MHz$^{-\gamma}$cm^{-1} and $\gamma = 2.5$. Nevertheless, the properties of the exciting light pulse (delta function light pulse) and detectors (point detectors with centre frequency 2.25 MHz and 70% bandwidth) were kept as constants. The first combination of α_0 and γ is similar to that of the breast tissue. The second and third combinations produce higher attenuation. In the fourth case, detectors with finite size were utilized to capture the PA signals. The diameter (line element in 2D) of the detectors was fixed to 6 mm but the width of the Gaussian apodization was successively changed, $\sigma = 0.6$, 2.0 and 5.0 mm. Other parameters remained unaltered (i.e. delta function light pulse, point detectors with centre frequency 2.25 MHz and 70% bandwidth, and acoustically lossless and nondispersive medium). The same simulations were also conducted for 12 mm sensors.

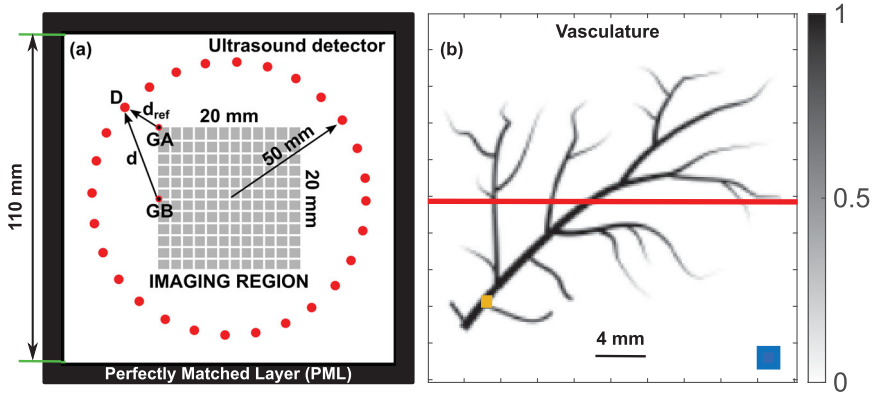

Figure 1. (a) Schematic of the PA simulation geometry in 2D; 80 sensors have been uniformly placed around the imaging region with 50 mm as the scanning radius. (b) Demonstration of the vasculature phantom. The regions inside the yellow and blue boxes have been considered as the region of interest ('roi') and the background area ('back'). The PA pressure data of these sectors have been utilized for computing the signal to noise ratio of the reconstructed images. The numerical values of the pixels along the red line of the source phantom and the reconstructed images have been compared.

3.2. Implementation of BP, MBP and ITR algorithms

Equation (6) was directly utilized for point detectors for image reconstruction by the BP algorithm. The ITR technique is a reconstruction method offered by the k-Wave toolbox. For finite sensors, each detector was divided into a number of points (51 points for 6 mm sensor and 101 points for 12 mm transducer). Each point represented an ideal point detector and pressure data at such points were stored during the forward simulation. Equation (8) was used to calculate the resultant signal for each detector. The BP algorithm was then applied using the resultant signals. In the case of MBP, a resultant signal (recorded by a detector) was redistributed in the same Gaussian manner over those points and after that, the BP scheme was followed [23,34].

3.3. Building of system matrix

The TH and TV are system matrix based reconstruction protocols. The PA pressure data corresponding to 1500 time points (from 1001 to 2500) were used for constructing the A matrix as well as for image reconstruction. The sizes of matrices became: A matrix – $m \times n = 120000 \times 40401$, z matrix – 40401×1 and b matrix – $m = 120000 \times 1$. The details of the construction of A are as follows. Consider that the PA signal [denoted by $\psi_{\mathrm{GA}}(t)$] produced by a corner pixel GA (top left most corner) and detected at D was (see Figure 1a). This signal was treated as the reference signal. The PA signal emitted by a point GB could be estimated to be (*via* the scaling and shifting properties of the PA signal),

$$\psi_{\mathrm{GB}}(t) = \sqrt{\frac{d_{ref}}{d}} \times F^{-1}\left[F[\psi_{\mathrm{GA}}(t)] \times e^{i\frac{\omega}{v}(d-d_{ref})}\right], \tag{19}$$

where F and F^{-1} are the forward and inverse Fourier transform operators; d_{ref} and d are the distances of the grid points GA and GB from D, respectively. The multiplication has to be performed element wise. Equation (19) allowed us to calculate the PA signals generated by all grid points (traversing column-wise starting from the top left most corner) and recorded at D. Those signals were appended in the A matrix – rows from 1 to 1500 and columns from 1 to 40401. The signals to other detectors could also be determined and loaded into the A matrix. In the first case, the finite width of the laser pulse was considered while calculating $\psi_{\mathrm{GA}}(t)$. Similarly, in the second case, the bandwidth of the detectors was also included within the forward simulation providing realistic $\psi_{\mathrm{GA}}(t)$. The time taken to build the A matrix for these cases was about 15 minutes. The algorithm for building the A matrix for point detectors is presented in Algorithm 1.

In the third type of simulation, the medium was chosen to be acoustically lossy and dispersive. The signal for GB could be computed from that of GA as

$$\psi_{\mathrm{GB}}(t) = \sqrt{\frac{d_{ref}}{d}} \times F^{-1}\Big[F[\psi_{\mathrm{GA}}(t)] \times e^{i(d-d_{ref})[\frac{\omega}{v}+i\alpha_0(|\omega|^{\gamma}-i\tan(\pi\gamma/2)\ \omega|\omega|^{\gamma-1})]}\Big]. \tag{20}$$

Therefore, in this case also the PA signals for all pixels were computed for all detector locations and hence, were loaded into the A matrix. The execution time to form the A matrix for this case was approximately 1 hour and 20 minutes in the same virtual machine. The algorithm is given in Algorithm 1.

Algorithm 1: Building of the system matrix **A** for ideal point detectors.

Input: The position coordinates of the corner grid (x_{gref} and y_{gref}) and the reference detector (x_{dref} and y_{dref}); speed of sound (v); position coordinate array for all grid points (x_g and y_g); position coordinate array for all detectors (x_d and y_d)
Output: A matrix
Step 1: Generate the reference signal (ψ_{GA})
Step 2: Assign $LL \leftarrow$length of ψ_{GA}
Step 3: Calculate the reference distance
$d_{ref} = [(x_{dref} - x_{gref})^2 + (y_{dref} - y_{gref})^2]^{\frac{1}{2}}$
Step 3: for $j = 1, 2, ...,$ length of x_d do steps R1- -R3
R1: $N_s \leftarrow (j-1) \times LL + 1$
R2: $N_f \leftarrow j \times LL$
R3: for $k = 1, 2, ...,$ length of x_g do steps i-iv
i. Compute
$d = [(x_d(j) - x_g(k))^2 + (y_d(j) - y_g(k))^2]^{\frac{1}{2}}$
ii. Estimate ψ using Equation (19) for nonabsorbing medium
iii. Estimate ψ using Equation (20) for absorbing and dispersive medium
iv. for $u = N_s, ..., N_f$ do step a
a. $A(u,k) \leftarrow \psi(u + 1 - N_s)$

The A matrix for finite detectors was created in the following manner (i.e. for the fourth type of simulation). At first, the PA signal emitted by a corner grid and detected at a point lying on a detector was computed and stored. The next step was to compute the PA signals at all the points (e.g. 51 points for a 6-mm detector and 101 points for a 12-mm detector) of that detector using

Equation (19). Such signals (with appropriate Gaussian weights) were summed up to obtain the resultant signal. In this way, the PA signals for all grid points at that detector could be calculated and assigned to the A matrix. This step was repeated for other detectors. Algorithm 2 summarizes this algorithm. The computation time for the construction of the A matrix was approximately 2 hours and 4 hours, for 6 mm and 12 mm transducers, respectively.

Algorithm 2: **A** matrix formation for finite detectors.

Input: The position coordinates of the corner grid (x_{gref} and y_{gref}) and the reference detector (x_{dref} and y_{dref}); speed of sound (v); position coordinate array for all grid points (x_g and y_g); position coordinate array for centers of all detectors (x_d and y_d); position coordinate array for all elements of all detectors (x_{del} and y_{del}); number of point elements in each finite detector (N_{el}); diameter of the detector ($diaD$)

Output: A matrix

Step 1: Compute $dl = diaD/(N_{el} - 1)$

Step 2: Compute $N_{mel} = floor(N_{el}/2) + 1$

Step 3: Generate the reference signal (ψ_{GA})

Step 4: Assign $LL \leftarrow$length of ψ_{GA}

Step 5: Calculate the reference distance,

$$d_{ref} = [(x_{dref} - x_{gref})^2 + (y_{dref} - y_{gref})^2]^{\frac{1}{2}}$$

Step 6: for $j = 1, 2, ...,$ length of x_d do steps R1- -R3

R1: $N_s \leftarrow (j - 1) \times LL + 1$

R2: $N_f \leftarrow j \times LL$

R3: for $k = 1, 2, ...,$ length of x_g do steps i- -iii

i. Declare a vector ψ_{new} of the same length of ψ and initialize with 0s

ii. for $el = 1, 2, \ldots, N_{el}$ do steps S1- -S5

S1. Compute W using Equation (9)

S2. Assign $mn \leftarrow (j - 1) \times N_{el} + el$

S3. Compute

$$d = [(x_{del}(mn) - x_g(k))^2 + (y_{del}(mn) - y_g(k))^2]^{\frac{1}{2}}$$

S4. Estimate ψ using Equation (19) for nonabsorbing medium

S5. $\psi_{new} \leftarrow \psi_{new} + W \times \psi$

iii. for $u = N_s, ..., N_f$ do step a

a. $A(u, k) \leftarrow \psi_{new}(u + 1 - N_s)$

3.4. Implementation of the TH and TV algorithms

The image formation was accomplished subsequently. The regularization toolbox was used for the TH scheme [36]. The total time for the singular value decomposition and image reconstruction was nearly 3 hours 30 minutes for the point detectors. It took around 2 hours 30 minutes for the finite sensors in the same machine. The TVAL toolbox was utilized to implement Equation (13) for image creation. The numerical value of another penalty parameter β was given as an input to the function TV3. Various values of β were tried and the value providing the best-reconstructed image of a test source phantom was used in all simulations. The execution time for TV was $\approx$ 10 minutes for point detectors, around 17 minutes for 6 mm detectors and 20 minutes for 12 mm transducers.

3.5. Analysis of the reconstructed images

The quantitative values of various image quality parameters were then computed using Equations (14)–(18). The computations of the ERN and PCC were trivial. The pixels belonging to the source and the background regions were counted first in the ground truth image and subsequently, $n_{roi} = A_{roi}/A_{total}$ and $n_{back} = A_{back}/A_{total}$ were computed. The mean and the standard deviation of PA pressure were also estimated from these sets of pixels for the reconstructed image. After that, Equation (16) was evaluated to estimate the CNR for each reconstructed image. The 'roi' and 'back' regions contained 49 and 169 pixels, respectively (see orange and blue boxes, respectively in Figure 1b) and pressure values of these pixels were utilized to calculate the SNR of that 'roi' region of a reconstructed image. To estimate the SSIM of an image, we first fixed the scale (minimum and maximum pressure) and mapped the pressure values of both the images (ground truth and reconstructed) with respect to this scale. Then all the pressure values were normalized by the maximum pressure. Various pressure values of pixels varying from 0 (minimum pressure) to 1 (maximum pressure) were divided into 256 levels. This step was performed for both the images (ground truth and reconstructed). Thereafter, these images were given as the inputs into the ssim function of MATLAB and the numerical value of SSIM was obtained as the output.

4. Numerical results

4.1. PA signal estimation

Figure 2(a) shows that the PA signal (ψ_{GA}) simulated by the k-Wave toolbox for the corner pixel (source) and detected by a point sensor located at a distance $d_{ref} = 3.6$ cm from the source (see Figure 1a). Figure 2(b) displays the PA signals generated by the k-Wave and Equation (19) when the source to detector distance is $d = 6.4$ cm. The coupling medium is acoustically lossless. These two signals (for ψ_{GB}) exhibit a perfect match. Similarly, ψ_{GA} provided by the k-Wave toolbox for lossy

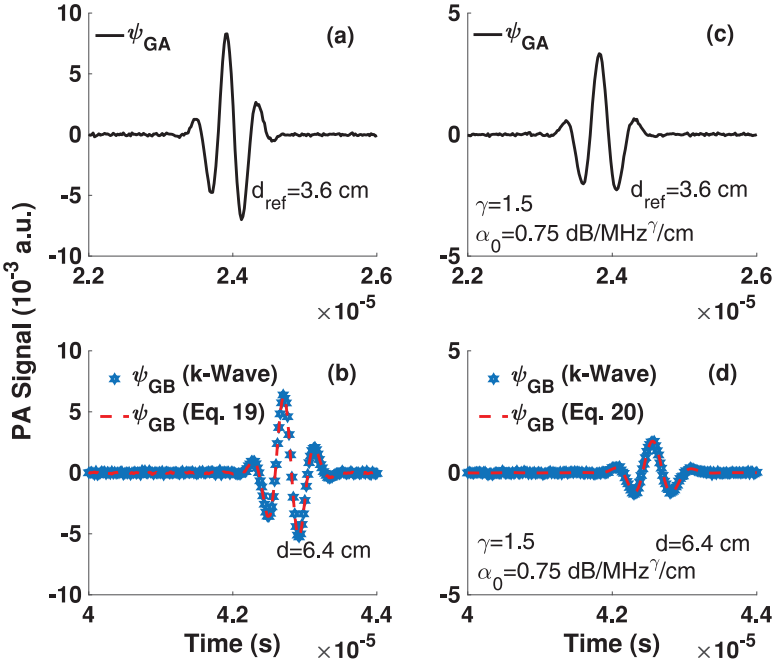

Figure 2. (a) PA signal generated by the k-Wave toolbox for an acoustically lossless medium and when source to detector distance is $d_{ref} = 3.6$ cm. (b) Plots of the PA signals generated by the k-Wave toolbox and Equation (19) for the same medium but source to detector distance is $d = 6.4$ cm. (c) Same as (a) but for an acoustically lossy and dispersive medium with $\alpha_0 = 0.75$ dB MHz$^{-\gamma}$ cm^{-1} and $\gamma = 1.5$. (d) Same as (b) but for the lossy and dispersive medium and Equation (20) has been used to calculate ψ_{GB}.

and dispersive medium with $\alpha_0 = 0.75\,\text{dB/MHz}^{\gamma}/\text{cm}$ and $\gamma = 1.5$ is plotted in Figure 2(c). In this case, $d_{ref} = 3.6$ cm. The computed PA signals (ψ_{GB}) for the k-Wave and Equation (20) shown in Figure 2(d) look identical when the source and the detector are separated by $d = 6.4$ cm. Figure 2 confirms that Equation (19) and Equation (20) can be used for estimating the PA signals during the system matrix formation.

4.2. Variation of pulse width

The reconstructed images for different pulse widths of the incident laser beam are shown in Figure 3. Each image is normalized with respect to its maximum pixel value. All the reconstruction algorithms discussed above have been utilized. The regularization parameter λ used in the TH method is placed on the top of each image in the third column. The penalty parameters η and β for the TV scheme are provided on the top of the respective images. The width of the excitation pulse is 300 ns in the case of Figures 3(a–d). The line plots for these methods along the red line (as shown in Figure 1b) are given in Figure 3(e). The same line plot for the source image is also drawn in this figure for comparison.

Similarly, the reconstructed images and line plots for two other pulses (with widths 600 and 900 ns) are included in Figures 3(f–j) and Figures 3(k–o), respectively. Figures 3(a, f and k) clearly depict that blurring enhances with the expansion of the excitation light pulse. This is true for Figures 3(b, g and l) as well. The BP and ITR schemes are not able to reproduce the structure of the vasculature faithfully. Uniform background noise is present in the BP images whereas it is less prominent in the ITR images at least at the boundaries. Figures 3(c, h, m, d, i , n) demonstrate that the TH and TV provide a significantly better reconstruction of the initial pressure map in all cases. The TH images also have uniform background noise but it is comparatively less than the BP and ITR images. The TV performs far better than the other algorithms. The line plots for the BP and ITR methods (dash-dash and dot-dot lines, respectively) deviate greatly from the source line (black line) but those of the TH and TV techniques (red circle and green diamond, respectively) match well with the source line.

The numerical values of the parameters quantifying the performance of these algorithms are given in Table 1 (rows 4–8). The numerical value of ERN in general increases as the pulse width of the laser beam increases for the BP algorithm (second, sixth and tenth columns and fourth row of Table 1). This is obvious because blurring increases for broader laser pulses. The PCC decreases from 0.45 to −0.20 when the width of the laser pulse changes from 300 to 900 ns, respectively (see row 5, columns 2 and 10); CNR and SSIM also follow the same trend. Their values go down from 0.48 and 0.34

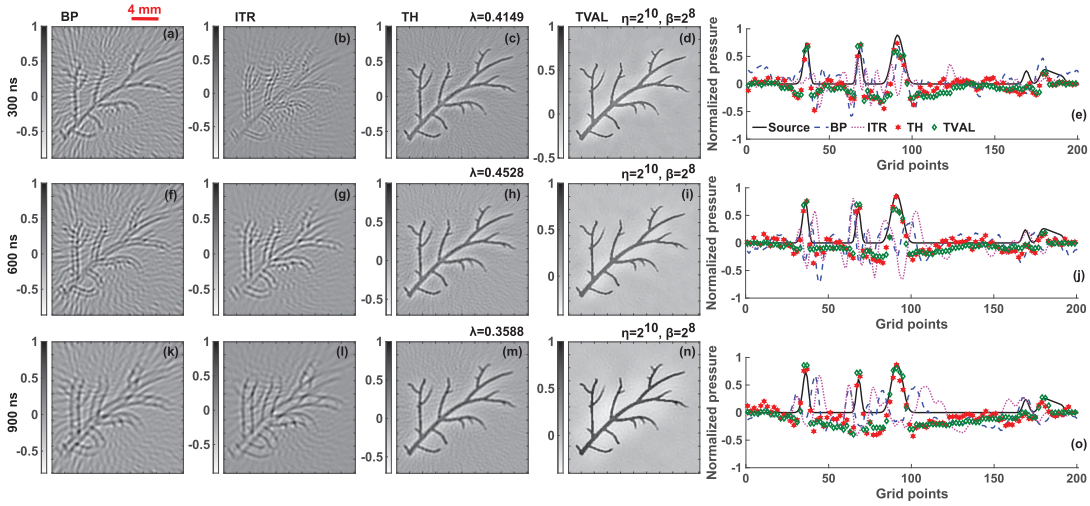

Figure 3. (a)–(d) Reconstructed images of the vasculature phantom for the BP, ITR, TH and TV algorithms, respectively, using ideal point detectors when 300 ns laser pulse is used to excite the tissue. Each image is normalized by its maximum pixel value. (e) The variation of normalized pressure for each image along the red line (as shown in Figure 1b). (f–j) Same as (a–e) but for the 600 ns input laser pulse, respectively. (k–o) Same as (a–e) but for the 900 ns incident laser pulse, respectively.

Table 1. Quantitative analysis of the performance of various reconstruction algorithms based upon some standard parameters in cases of the finite laser pulse (rows 1–8), finite bandwidth of detectors (rows 9–16) and for different attenuating media (rows 17–25). The unit of SNR is dB.

	Pulse width											
	300 ns				**600 ns**				**900 ns**			
Metric	**BP**	**ITR**	**TH**	**TV**	**BP**	**ITR**	**TH**	**TV**	**BP**	**ITR**	**TH**	**TV**
ERN	38.24	40.50	29.79	26.54	51.72	50.91	26.17	21.49	49.33	49.08	25.10	26.50
PCC	0.45	0.07	0.66	0.74	–0.06	–0.27	0.74	0.84	–0.20	–0.27	0.79	0.85
SNR	15.13	17.22	20.96	30.66	14.27	14.12	22.63	34.10	16.10	16.61	24.49	36.50
CNR	0.48	0.40	0.50	0.74	0.47	-0.10	0.80	1.12	–0.05	–0.53	1.05	1.18
SSIM	0.34	0.47	0.52	0.85	0.17	0.44	0.58	0.88	0.27	0.47	0.63	0.87
	Bandwidth											
	30%				**50%**				**90%**			
Metric	**BP**	**ITR**	**TH**	**TV**	**BP**	**ITR**	**TH**	**TV**	**BP**	**ITR**	**TH**	**TV**
ERN	47.77	42.99	41.54	40.68	42.86	40.47	32.28	28.49	27.57	32.21	19.54	9.79
PCC	0.27	0.18	0.41	0.52	0.38	0.28	0.59	0.75	0.68	0.54	0.87	0.96
SNR	14.43	18.31	22.13	34.64	16.17	21.61	23.43	33.92	19.60	28.06	26.52	34.58
CNR	0.33	0.25	0.52	0.70	0.57	0.49	1.00	1.48	1.65	1.36	2.48	3.07
SSIM	0.34	0.62	0.49	0.76	0.37	0.64	0.60	0.87	0.44	0.68	0.60	0.91
	Absorption parameters											
	$\alpha_0 = 0.75$**dB/MHz$^\gamma$/cm**				$\alpha_0 = 5.75$**dB/MHz$^\gamma$/cm**				$\alpha_0 = 3.75$**dB/MHz$^\gamma$/cm**			
	$\boldsymbol{\gamma = 1.5}$				$\gamma = 1.5$				$\gamma = 2.5$			
Metric	**BP**	**ITR**	**TH**	**TV**	**BP**	**ITR**	**TH**	**TV**	**BP**	**ITR**	**TH**	**TV**
ERN	47.62	30.99	24.27	21.91	48.91	29.95	19.71	28.28	28.17	28.54	28.33	32.54
PCC	0.12	0.60	0.79	0.86	-0.04	0.63	0.83	0.68	0.65	0.65	0.66	0.64
SNR	10.31	32.32	26.14	35.51	21.18	53.83	31.17	53.74	32.72	50.10	21.32	60.34
CNR	0.62	1.72	2.09	2.32	-0.05	2.30	3.52	2.43	2.43	2.37	2.31	2.21
SSIM	0.17	0.72	0.62	0.90	0.50	0.74	0.63	0.75	0.68	0.75	0.30	0.74

to –0.05 and 0.27, respectively (see rows 7 and 8, columns 2 and 10). The SNR values exhibit negligible variation for the three cases. Similar observations can be made for the ITR scheme. The numerical values of these parameters, in general, suggest that the BP algorithm has a slight edge over the ITR scheme. The quantitative estimates for the figures of merit for the TH and TV protocols exhibit small variation and remain on the higher side [e.g. PCC = 0.85, SNR = 36.50 dB and SSIM = 0.87 for the TV scheme at 900 ns laser pulse (see column 13, rows 5, 6 and 8)] providing faithful reconstructed images independent of the pulse width of the input laser.

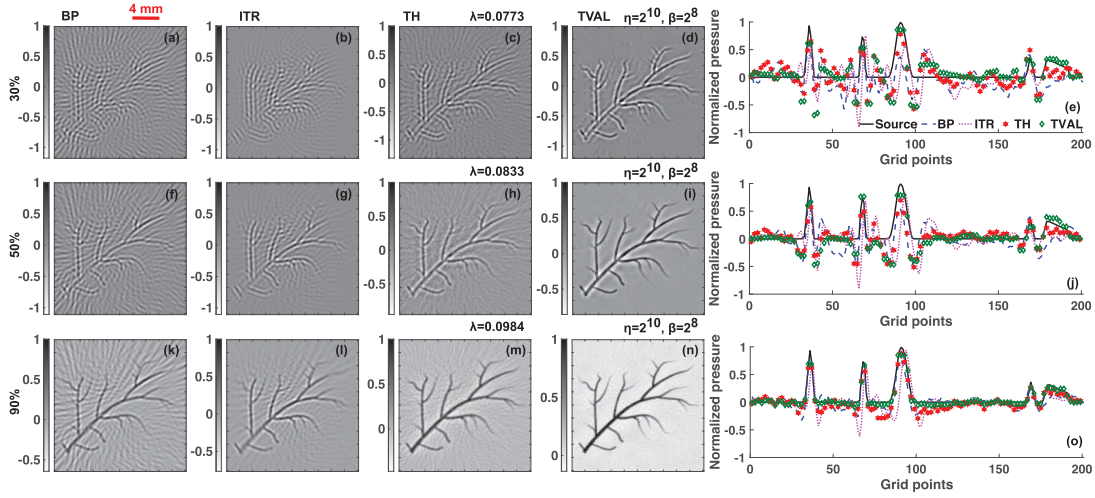

Figure 4. (a)–(d) Normalized reconstructed images of the vasculature phantom for the BP, ITR, TH and TV methods, respectively for ideal point detectors with 30% bandwidth. (e) Plots of normalized pressure of the reconstructed images and of the ground truth along a horizontal line (red line in Figure 1b). (f)–(j) and same as (a)–(e) but for detectors with 50% bandwidth, respectively. (k)–(o) Same as (a)–(e) but for sensors with 90% bandwidth, respectively.

4.3. Variation of bandwidth

The first row of Figure 4 displays the images of the vasculature phantom reconstructed by the four methods as stated above for 30% bandwidth of the detectors. The delta light pulse was used to excite the region of interest. The second and third rows represent the reconstructed images mapped from the PA signals captured by detectors with 50% and 90% bandwidths, respectively. Figures 4(e, j, o) are the line plots for these images along the same horizontal line as for Figure 3.

Prominent image blurring can be seen for 30% bandwidth in all the cases. In general, no method is able to reconstruct the ground truth faithfully. This is also evident from Figure 4(e). Image reconstruction improves for each method as the detection bandwidth increases. The pressure distribution inside the source is better mimicked in these cases (see Figures 4j and o) than that of Figure 4(e). Background noise appears in a similar manner as discussed in the previous case (Figure 3). As expected, the contrast in the images improves with increasing transducer bandwidth. The TH and TV techniques perform better than the BP and ITR methods at each level of bandwidth.

Table 1 (rows 12–16) presents the estimated values of the metrics. The numerical values of the metrics demonstrate expected changes as the bandwidth grows from 30% to 90% for the BP and ITR models. For example, ERN decreases from 47.77 to 27.57, PCC increases from 0.27 to 0.68, SSIM varies from 0.34 to 0.44 for the BP technique (see columns 2 and 10, rows 12, 13 and 16), whereas ERN drops from 42.99 to 32.21, PCC rises from 0.18 to 0.54, SSIM changes from 0.62 to 0.68 for the ITR formalism (see columns 3 and 11, rows 12, 13 and 16). The corresponding values for the TH framework always remain at the higher levels for each bandwidth condition showing that better image reconstruction is possible using this technique and those of the TV procedure attains the highest values establishing that it is the best image reconstruction technique [e.g. PCC = 0.96, CNR = 3.07, SSIM = 0.91, etc. (see column 13, rows 13, 15, 16)].

4.4. Variation of medium attenuation

The frequency-dependent acoustic attenuation (accompanied by dispersion) is another source of blurring in the reconstructed images. Three different cases have been analysed. The reconstructed images for the vasculature phantom obtained for the three settings of the attenuation parameters are arranged in the first, second and third rows, respectively in Figure 5. The line plots are presented in the fifth column. Figure 5(a) shows that the BP method fails to remove blurring. However, the other methods provide relatively less blurry images (see Figures 5 b–d). In fact, blurring decreases as we move from left to right. Figure 5(e) also exhibits the same trend. Contrast decreases and blurring increases as the acoustic attenuation increases (see rows 2 and 3). In other words, the heights of the amplitudes decrease and widths of the branches increase (see Figures 5 j and o).

The quantitative comparison of the algorithms is given in Table 1 (rows 21–25). The computed values for the BP algorithm are shown in the second column (for the first attenuating medium) and they are in general in the

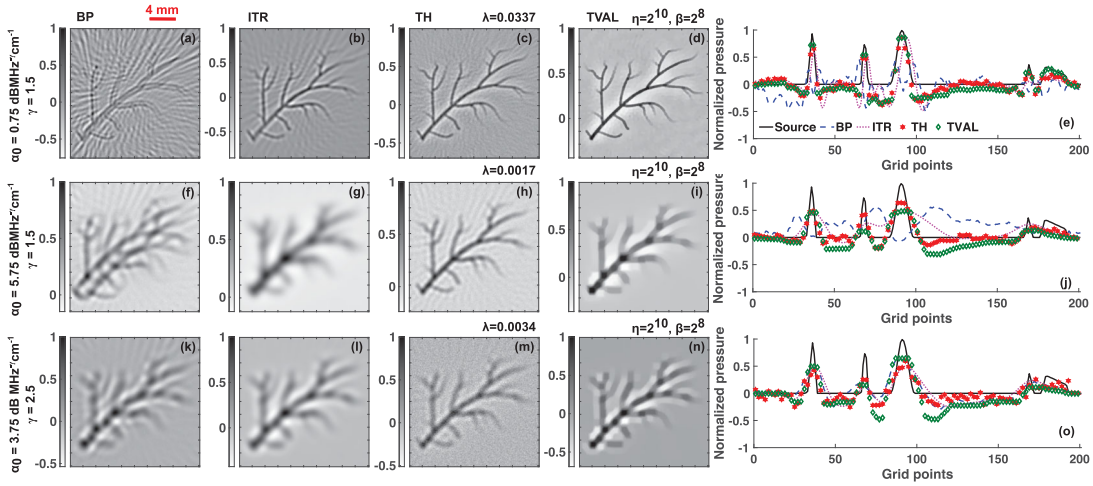

Figure 5. (a)–(d) Image reconstruction of the vasculature phantom by the BP, ITR, TH and TV algorithms, respectively for $\alpha_0 = 0.75$ dB/MHz$^{\gamma}$/cm, $\gamma = 1.5$ and for ideal point detectors. (e) Plots of normalized pressure along the red line (see Figure 1b) for the source and the reconstructed images. (f)–(j) Same as (a)–(e) but for $\alpha_0 = 3.75$ dB/MHz$^{\gamma}$/cm, $\gamma = 1.5$, respectively. (k)–(o) Same as (a)–(e) but for $\alpha_0 = 5.75$ dB/MHz$^{\gamma}$/cm, $\gamma = 2.5$, respectively.

lower side due to image blurring. The ITR method works better than the BP method in this case (third column). For example, the PCC and SSIM for the ITR method are about 5 and 4 times higher than those of the BP algorithm (rows 22 and 25, columns 2 and 3, Table 1). The numerical values for the ITR technique remain similar for the second and third media (columns 7 and 11, Table 1). The TV algorithm performs marginally better than the TH scheme. The numerical values of SNR and CNR have increased significantly because of noise-cleaning owing to attenuation (rows 23 and 24; columns 4 and 5, 8 and 9, 12 and 13, Table 1).

4.5. Variation of sensor apodization

Reconstructed images with different Gaussian apodizations are portrayed in Figure 6 for the 6 mm transducers. As expected, blurring increases as the width of the Gaussian apodization increases (i.e. strong to weak apodization). It is clear from the BP images (see Figures 6a, f, k). Blurring as well as background noise levels are comparatively less in the images generated by the MBP algorithm (see Figure 6 b, g, l). In addition to blurring, tangential resolution degrades when we move radially outward from the centre of the reconstructed image. It is interesting

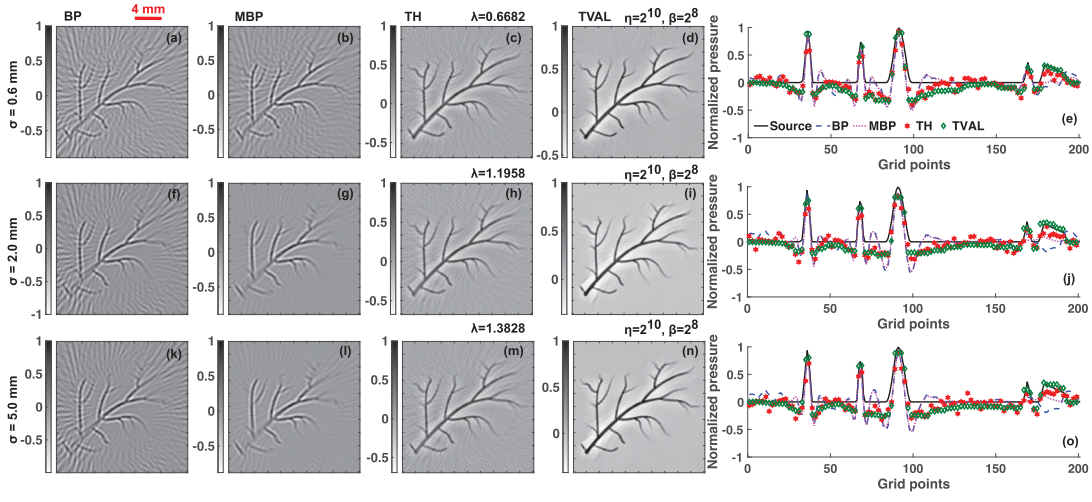

Figure 6. (a)–(d) Simulated images by the BP, ITR, TH and TV techniques, respectively for the vasculature phantom using finite-size detectors with $\sigma = 0.6$ mm and 6 mm as the diameter of each transducer. (e) Plot of the image profile along the red line (as drawn in Figure 1b) for each algorithm. (f)–(j) Same as (a)–(e) but for $\sigma = 2.0$ mm, respectively. (k)–(o) Same as (a)–(e) but for $\sigma = 5.0$ mm, respectively.

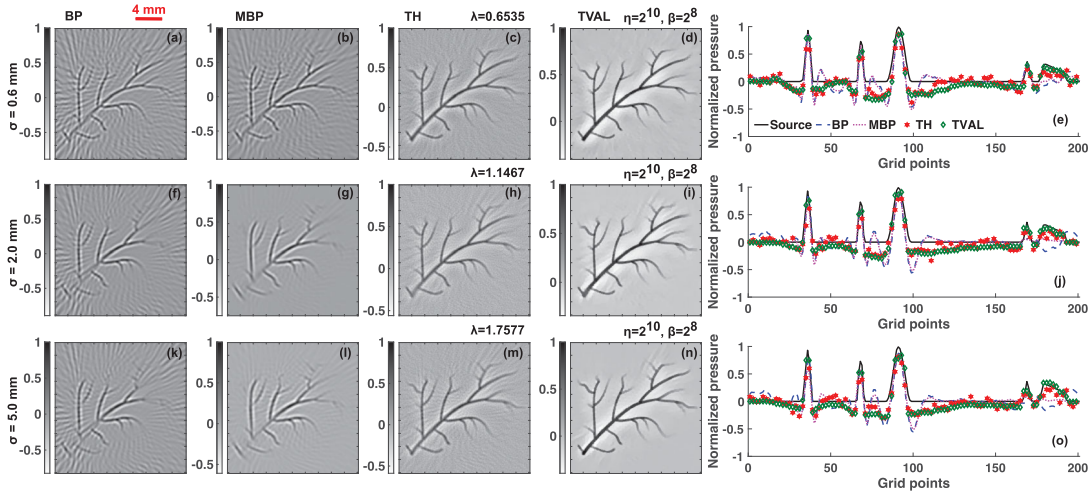

Figure 7. (a–d) Reconstructed images of the vasculature phantom for the BP, ITR, TH and TV protocols, respectively for finite-size detectors with $\sigma = 0.6$ mm and 12 mm as the diameter of each transducer. (e) The variation of normalized pressure along the red line (as drawn in Figure 1b) for the source and reconstructed images. (f–j) Same as (a)–(e) but for $\sigma = 2.0$ mm, respectively. (k–o) Same as (a–e) but for $\sigma = 5.0$ mm, respectively.

Table 2. Comparison of the performance metrics for the evaluation of the reconstruction techniques for different apodization conditions (rows 1–8 for 6 mm transducer and rows 9–16 for 12 mm transducer). The unit of SNR is dB.

	Sensor diameter (6 mm)											
	$\sigma = 0.6$**mm**				$\sigma = 2.0$**mm**				$\sigma = 5.0$**mm**			
Metric	**BP**	**MBP**	**TH**	**TV**	**BP**	**MBP**	**TH**	**TV**	**BP**	**MBP**	**TH**	**TV**
ERN	36.11	31.31	26.07	24.38	36.38	28.34	24.70	20.03	36.32	28.53	25.08	21.22
PCC	0.53	0.62	0.76	0.84	0.50	0.65	0.78	0.88	0.49	0.64	0.77	0.88
SNR	15.00	20.25	21.89	42.74	18.59	26.40	20.77	55.59	19.21	24.92	21.38	53.45
CNR	1.04	1.27	1.73	1.91	1.03	1.40	1.87	2.28	1.00	1.38	1.83	2.26
SSIM	0.41	0.56	0.57	0.91	0.45	0.81	0.56	0.93	0.46	0.79	0.55	0.93
	Sensor diameter (12 mm)											
	$\sigma = 0.6$**mm**				$\sigma = 2.0$**mm**				$\sigma = 5.0$**mm**			
Metric	**BP**	**MBP**	**TH**	**TV**	**BP**	**MBP**	**TH**	**TV**	**BP**	**MBP**	**TH**	**TV**
ERN	36.00	31.29	25.04	21.26	35.11	27.70	23.60	18.58	35.79	27.11	24.14	20.37
PCC	0.53	0.62	0.77	0.87	0.48	0.66	0.79	0.90	0.44	0.68	0.78	0.88
SNR	15.15	20.36	23.33	41.34	19.07	36.49	19.51	52.65	19.27	29.16	21.87	50.29
CNR	1.04	1.27	1.80	2.16	1.01	1.49	2.02	2.51	0.95	1.59	1.97	2.29
SSIM	0.42	0.56	0.58	0.92	0.49	0.85	0.58	0.93	0.48	0.82	0.59	0.93

to note that blur-free image reconstruction is possible using the TH and TV protocols. The TV images are even better (with respect to contrast) than those of the TH method. This is consistent with Figures 6(e, j, o). The same images for the 12 mm transducers are given in Figure 7.

Table 2 (rows 4–8) presents a quantitative comparison of the performance of the reconstruction algorithms for the 6 mm transducers. The corresponding numerical values of the figures of merit are included in Table 2 (rows 12–16) for the 12 mm transducers. The image quality degrades (PCC decreases from 0.53 to 0.49) as the σ increases from 0.6 to 5 mm in the case of the BP technique (see row 5, columns 2 and 10, Table 2). Other parameters exhibit small fluctuations. MBP works always better than the conventional BP protocol for all apodization conditions. For instance, CNR and SSIM can be found to be approximately 38% and 71% higher for the MBP technique compared to the BP approach in the case of $\sigma = 5.0$ mm (see rows 7 and 8, columns 10 and 11, Table 2). The numerical values for the TH and TV procedures do not differ significantly, though the apodization parameter alters. PCC, CNR and SSIM can be seen to be more than 0.75, 1.70, and 0.5, respectively for the TH scheme for all cases (see rows 5, 7, and 8 and columns 4, 8, and 12, Table 2). Those values for the TV method are 0.80, 1.90, and 0.9, respectively (see rows 5, 7, and 8 and columns 5, 9, and 13, Table 2). The numerical values of the metrics appear almost identical for the 12 mm transducer with respect to the 6 mm sensor (rows 12–16, Table 2).

5. Discussion and conclusion

In this work, we presented a robust method for deblurring the PAT images. A blood vessel network was utilized as a gray scale source image (absorption coefficient/initial pressure was $\neq 0$ for the black regions and 0 for the white background). The image reconstruction was performed using the BP, ITR, TH and TV techniques when point detectors were used to record the PA signals. In the case of finite size apodized transducers, MBP instead of ITR was used along with the other reconstruction algorithms. All the simulations were performed using the k-Wave toolbox in the MATLAB environment. The additional packages like the regularization toolbox and TV toolbox were also integrated with the MATLAB to carry out the reconstructions for the TH and TV techniques, respectively.

Effects of four factors (inducing blurring) typically present in a PAT system were investigated. As stated earlier, these factors were (i) finite width of the incident laser pulse, (ii) finite bandwidth of the detectors, (iii) acoustically absorbing and dispersive coupling medium through which PA waves propagate and (iv) transducers with finite-size apertures with Gaussian sensitivity profile. Only a single factor was studied at a time. We systematically examined how the reconstructed images, created by the reconstruction algorithms, would appear in presence of each factor. After that, we evaluated whether a reconstruction procedure could rectify the limitation/limitations of the imaging system and facilitate distortion-free output image.

The BP techniques essentially assume that the detectors are the ideal point detectors and subsequently, implement the delay and sum algorithm. Hence, it does not have any internal mechanism to correct the distortions induced by the imaging system. The same is also true for the ITR algorithm. Therefore, it is expected that these algorithms cannot overcome the limitation/limitations of the imaging system while performing the image reconstruction. In the case of model matrix approaches considered in this study, the model matrix was built by loading the PA signals emitted by each grid point and recorded at each detector location. Therefore, the factor/factors responsible for image blurring was/were included within the model matrix. After that, the image reconstruction was accomplished through model matrix inversion. The model matrix inversion can be thought of as a deconvolution operation. It can be speculated that the system-dependent parameters are cancelled out during this procedure and thus blur-free reconstructed images can be obtained.

It may be emphasized here that this approach can easily be implemented in practice by constructing the A matrix using the PA signal emitted by a point source (e.g. black lead) and detected by the transducer which will be used for scanning. This will serve as the reference signal. Thereafter, Equation (19) or Equation (20) can be utilized to estimate the PA signals for different grid points and at different detector positions. This approach may fail to provide faithful image reconstruction for acoustically inhomogeneous imaging regions (i.e. when the speed of sound is different at different spatial locations). Moreover, in the future, it would be interesting to conduct a similar study with a numerical phantom containing many gray levels, which may help to develop further insights into the problem.

In this work, for the first time as far as we know, the system matrix was constructed for transducers with apertures of finite size and nonuniform sensitivity profile. This was possible because a finite sensor (a line segment in the case of two dimensions) was modelled as a collection of discrete points. The PA signals recorded by those points were summed up, with Gaussian weights to incorporate the apodization effect, to obtain the resultant signal captured by that transducer. The Gaussian apodization is often used in ultrasonic imaging to suppress the artefacts arising from the sidelobes and this issue has been extensively studied in ultrasonic imaging [*40*]. The system matrix was constructed utilizing such signals. Nevertheless, these point sensors were considered omnidirectional and thus the effect of directivity of finite transducers was not incorporated in this work.

In conclusion, a method involving the system matrix approach is discussed to provide a blur-free PAT imaging. The robustness of the method is established through numerical simulations. Future work will include experimental verification of the proposed method.

Acknowledgments

The authors would like to acknowledge BMIL, IIITA laboratory members for their continuous inputs; special thanks to Mr. Avijit Paul for participating in many stimulating discussions related to this work. The computational results reported in this work were performed on the Central Computing Facility of IIITA, Allahabad. This work was supported by the ICMR, India grant (# 56/2/2020-Hae/BMS).

Disclosure statement

The authors have no conflicts of interest to disclose.

Funding

This work was supported by the Indian Council of Medical Research (ICMR), Govt. of India, India grant (# 56/2/2020-Hae/BMS).

References

[1] Wang LV, Yao J. A practical guide to photoacoustic tomography in the life sciences. Nat Meth. 2016;13(8):627–638.

[2] Na S, Russin JJ, Lin L, et al. Massively parallel functional photoacoustic computed tomography of the human brain. Nat Biomed Eng. 2021;1–9.

[3] Ron A, Deán-Ben XL, Gottschalk S, et al. Volumetric optoacoustic imaging unveils high-resolution patterns of acute and cyclic hypoxia in a murine model of breast cancer. Cancer Res. 2019;79(18):4767–4775.

[4] Prakash J, Kalva SK, Pramanik M, et al. Binary photoacoustic tomography for improved vasculature imaging. J Biomed Opt. 2021;26(8):086004.

[5] Huang S, Blutke A, Feuchtinger A, et al. Functional multispectral optoacoustic tomography imaging of hepatic steatosis development in mice. EMBO Mol Med. 2021;13(9):e13490.

[6] Xu M, Wang LV. Universal back-projection algorithm for photoacoustic computed tomography. Phys Rev E. 2005;71(1):016706.

[7] Treeby BE, Cox BT. k-wave: MATLAB toolbox for the simulation and reconstruction of photoacoustic wave fields. J Biomed Opt. 2010;15(2):021314.

[8] Burgholzer P, Matt GJ, Haltmeier M, et al. Exact and approximative imaging methods for photoacoustic tomography using an arbitrary detection surface. Phys Rev E. 2007;75(4):046706.

[9] Deán-Ben XL, Ntziachristos V, Razansky D. Acceleration of optoacoustic model-based 360 reconstruction using angular image discretization. IEEE Trans Med Imag. 2012;31(5):1154–1162.

[10] Wang K, Su R, Oraevsky AA, et al. Investigation of iterative image reconstruction in three-dimensional optoacoustic tomography. Phys Med Biol. 2012;57(17):5399–5423.

[11] Prakash R, Badal D, Paul A, et al. Photoacoustic signal simulation using discrete particle approach and its application in tomography. IEEE Trans Ultrason Ferroelectr Freq Control. 2021;68(3):707–717.

[12] Paul A, Warbal P, Mukherjee A, et al. Exploring polynomial based interpolation schemes for photoacoustic tomographic image reconstruction. Biomed Phys Eng Express. 2021; 8:015019.

[13] Wang Y, Xing D, Zeng Y, et al. Photoacoustic imaging with deconvolution algorithm. Phys Med Biol. 2004;49(14):3117–3124.

[14] Warbal P, Prakash R, Pramanik M, et al. Wiener filtering for deblurring of reconstructed images in photoacoustic tomography with finite size apodized transducers. IEEE Region 10 Conference (TENCON); IEEE; 2019. p. 96–101.

[15] Rajesh NA, Pullagurla H, Pramanik M. Deconvolution-based deblurring of reconstructed images in photoacoustic/thermoacoustic tomography. J Opt Soc Am A. 2013;30(10):1994–2001.

[16] La Riviere PJ, Zhang J, Anastasio MA. Image reconstruction in optoacoustic tomography for dispersive acoustic media. Opt Lett. 2006;31(6):781–783.

[17] Deán-Ben XL, Razansky D, Ntziachristos V. The effects of acoustic attenuation in optoacoustic signals. Phys Med Biol. 2011;56(18):6129–6148.

[18] Treeby BE. Acoustic attenuation compensation in photoacoustic tomography using time-variant filtering. J Biomed Opt. 2013;18(3):036008.

[19] Li M-L, Tseng Y-C, Cheng C-C. Model-based correction of finite aperture effect in photoacoustic tomography. Opt Express. 2010;18(25):26285–26292.

[20] Roitner H, Haltmeier M, Nuster R, et al. Deblurring algorithms accounting for the finite detector size in photoacoustic tomography. J Biomed Opt. 2014;19(5):056011.

[21] Van de Sompel D, Sasportas LS, Jokerst JV, et al. Comparison of deconvolution filters for photoacoustic tomography. PLoS ONE. 2016;11(3):e0152597.

[22] Pramanik M. Improving tangential resolution with a modified delay-and-sum reconstruction algorithm in photoacoustic and thermoacoustic tomography. J Opt Soc Am A. 2014;31(3):621–627.

[23] Warbal P, Pramanik M, Saha RK. Impact of sensor apodization on the tangential resolution in photoacoustic tomography. J Opt Soc Am A. 2019;36(2):245–252.

[24] Wang K, Ermilov SA, Su R, et al. An imaging model incorporating ultrasonic transducer properties for three-dimensional optoacoustic tomography. IEEE Trans Med Imaging. 2010;30(2):203–214.

[25] Warbal P, Saha RK. In silico evaluation of the effect of sensor directivity on photoacoustic tomography imaging. Optik. 2022;252:168305. in press.

[26] Chowdhury KB, Prakash J, Karlas A, et al. A synthetic total impulse response characterization method for correction of hand-held optoacoustic images. IEEE Trans Med Imaging. 2020;39(10):3218–3230.

[27] Shang R, Archibald R, Gelb A, et al. Sparsity-based photoacoustic image reconstruction with a linear array transducer and direct measurement of the forward model. J Biomed Opt. 2018;24(3):031015.

[28] Huang C, Wang K, Nie L, et al. Full-wave iterative image reconstruction in photoacoustic tomography with acoustically inhomogeneous media. IEEE Trans Med Imaging. 2013;32(6):1097–1110.

[29] Warbal P, Saha RK. Removal of blurring induced by band-limited transducers and broad laser pulse in photoacoustic tomography. European Conference on Biomedical Optics; Optical Society of America; 2021. p. ES1C-3.

[30] Okawa S, Hirasawa T, Kushibiki T, et al. Numerical evaluation of linearized image reconstruction based on finite element method for biomedical photoacoustic imaging. Opt Rev. 2013;20(5):442–451.

[31] Sheu YL, Li PC. Simulations of photoacoustic wave propagation using a finite-difference time-domain method with Berenger's perfectly matched layers. J Opt Soc Am A. 2008;124(6):3471–3480.

[32] Waters KR, Mobley J, Miller JG. Causality-imposed (Kramers–Kronig) relationships between attenuation and dispersion. IEEE Trans Ultrason Ferroelectr Freq Control. 2005;52(5):822–823.

[33] Kelly JF, McGough RJ, Meerschaert MM. Analytical time-domain Green's functions for power-law media. J Acoust Soc Am. 2008;124(5):2861–2872.

[34] Warbal P, Pramanik M, Saha RK. A robust modified delay-and-sum algorithm for photoacoustic tomography imaging with apodized transducers. European Conference on Biomedical Optics, Optical Society of America; 2019 Jun. p. 11077_38.

[35] Prakash J, Raju AS, Shaw CB, et al. Basis pursuit deconvolution for improving model-based reconstructed images in photoacoustic tomography. Biomed Opt Express. 2014;5(5):1363–1377.
[36] Hansen PC. Regularization tools version 4.0 for Matlab 7.3. Numer Algorithms. 2007;46(2):189–194.
[37] Li C, Yin W, Jiang H, et al. An efficient augmented Lagrangian method with applications to total variation minimization. Comput Optim Appl. 2013;56(3): 507–530.
[38] Song X, Pogue BW, Jiang S, et al. Automated region detection based on the contrast-to-noise ratio in near-infrared tomography. Appl Opt. 2004;43(5):1053–1062.
[39] Wang Z, Bovik AC, Sheikh HR, et al. Image quality assessment: from error visibility to structural similarity. IEEE Trans Image Process. 2004;13(4):600–612.
[40] Seo CH, Yen JT. Sidelobe suppression in ultrasound imaging using dual apodization with cross-correlation. IEEE Trans Ultrason Ferroelectr Freq Control. 2008;55(10): 2198–2210.